arXiv:1611.04402v1 [cond-mat.mtrl-sci] 14 Nov 2016

Impact of strain and morphology on magnetic properties of Fe_3O_4/NiO bilayers grown on Nb:$SrTiO_3$(001) and MgO(001)

O. Kuschel,[1] N. Pathé,[1] T. Schemme,[1] K. Ruwisch,[1] J. Rodewald,[1]
R. Buß,[1] F. Bertram,[2] T. Kuschel,[3,4] K. Kuepper,[1] and J. Wollschläger[1,*]

[1]*Department of Physics and Center of Physics and Chemistry of New Materials, Osnabrück University, 49076 Osnabrück, Germany*
[2]*DESY, Photon Science, 22607 Hamburg, Germany*
[3]*Center for Spinelectronic Materials and Devices, Department of Physics, Bielefeld University, 33615 Bielefeld, Germany*
[4]*Physics of Nanodevices, Zernike Institute for Advanced Materials, University of Groningen, 9747 AG Groningen, The Netherlands*

(Dated: November 15, 2016)

We present a comparative study on the morphology and structural as well as magnetic properties of crystalline Fe_3O_4/NiO bilayers grown on both MgO(001) and $SrTiO_3$(001) substrates by reactive molecular beam epitaxy. These structures are investigated by means of x-ray photoelectron spectroscopy, low energy electron diffraction, x-ray reflectivity and diffraction as well as vibrating sample magnetometry. While the lattice mismatch of NiO grown on MgO(001) is only 0.8 %, it is exposed to a lateral lattice mismatch of -6.9 % if grown on $SrTiO_3$. In the case of Fe_3O_4, the misfit strain on MgO(001) and $SrTiO_3$(001) amounts to 0.3 % and -7.5 %, respectively. To clarify the relaxation process of the bilayer system, the film thicknesses of the magnetite and nickel oxide films have been varied between 5 and 20 nm. While NiO films are well ordered on both substrates, Fe_3O_4 films grown on NiO/$SrTiO_3$ exhibit a higher surface roughness as well as lower structural ordering compared to films grown on NiO/MgO. Further, NiO films grow pseudomorphic in the investigated thickness range on MgO substrates without any indication of relaxation, whereas on $SrTiO_3$ the NiO films show strong strain relaxation. Fe_3O_4 films exhibit also strong relaxation even for films of 5 nm thickness on both NiO/MgO as well as on NiO/$SrTiO_3$. The magnetite layers on both substrates exhibit a fourfold magnetic in-plane anisotropy with magnetic easy axes pointing in ⟨110⟩ directions. Compared to growth on NiO/MgO, magnetite grown on NiO/$SrTiO_3$ shows strongly increased coercive fields due to higher density of structural defects.

PACS numbers:

I. INTRODUCTION

Transition metal oxides are one of the most interesting material classes providing a huge variety of structural, magnetic, and electronic properties ranging from metallic to insulating, from ferro- to antiferromagnetic, as well as ferroelectric states [1]. Especially, thin magnetite films (Fe_3O_4) [2] attracted intensive research interest in the last decade in the field of spintronics [3] and spin caloritronics [4]. Due to their anticipated half-metallic behavior with complete spin polarization at the Fermi level [5] and high (bulk) Curie temperature of 858 K [6], thin magnetite films are promising candidates for room temperature spintronic devices such as highly spin-polarized electrodes for magnetic tunneling junctions [7, 8] or spin-injectors [9]. Furthermore, multilayers of magnetite and platinum show huge thermoelectric effects [10] based on the recently observed spin Seebeck effect in magnetite [11] pushing the development of more efficient thermoelectric nanodevices [12].

Magnetite crystallizes in the inverse spinel structure with a lattice constant of 8.3963 Å [6] at 300 K. At ∼120 K it undergoes a metal-insulator transition (Verwey transition) [13] accompanied by a change from cubic to monoclinic crystal symmetry [14]. The reduction of the crystal symmetry leads to a spontaneous ferroelectric polarization and, thus, to multiferroicity [15, 16].

In order to control the relative magnetization alignment in magnetic tunnel junctions, exchange bias effects induced by additional antiferromagnetic layers are commonly used [17]. In case of Fe_3O_4 tunnel junctions, the antiferromagnetic NiO is a good candidate due to its small lattice mismatch of only 0.5 % and a high Néel temperature of 523 K [18].

Nickel oxide is an insulating material with a high thermal stability. It crystallizes in a rock salt structure with a lattice constant of 4.177 Å [19] at 300 K. In addition, NiO could be a key material for thermoelectric devices, since recently it was shown that NiO and other antiferromagnetic materials enhance the thermally induced spin currents in spin Seebeck effect experiments [20, 21].

Previous works [22–28] have focused on characterization of magnetite and nickeloxide films grown on MgO substrates because of the small lattice mismatch of 0.3 % and 0.8 %, respectively. However, it has recently been demonstrated that the electronic and magnetic properties of magnetite films can be modified using $SrTiO_3$ substrates [29, 30] in spite of the large lattice mismatch of

*Electronic address: jwollsch@uos.de

-7.5 %. For instance, one advantage using $SrTiO_3$ substrates is the possibility of doping and, thus, a tunable conductivity providing either an insulating or metallic substrate which could be used as bottom electrode in capacitor-like structures [16].

Fe_3O_4/NiO bilayer systems are attractive for magnetic tunnel junctions as well as for thermoelectric devices. Furthermore, bilayers grown on $SrTiO_3$ can be used to synthesize $Ni_xFe_{3-x}O_4$ thin films by thermally induced interdiffusion with tunable magnetic and electric properties [31]. Regarding Fe_3O_4/NiO bilayers, previous studies have focused on electronic structure, interfacial coupling and magnetic characterization [32–35] whereas to the best of our knowledge, there are no detailed structural studies for bilayers on $SrTiO_3$. However, the magnetic and transport characteristics of such films are sensitive to structural variations, number of defects or stoichiometric deviations and could be affected by the strain between the film and substrate. Therefore, in this work a comparative study on the growth, structural and magnetic properties of Fe_3O_4/NiO bilayers grown on MgO(001) and Nb-doped $SrTiO_3$(001) is presented.

Directly after deposition, the stoichiometry in the surface near region and the surface structure of each layer was determined *in situ* using x-ray photoelectron spectroscopy (XPS) and low energy electron diffraction (LEED), respectively. The bulk structure was investigated *ex situ* by x-ray reflectivity (XRR) and synchrotron radiation x-ray diffraction (SR-XRD) measurements and analyzed within the full kinematic diffraction theory. Further, magnetic properties, e.g., magnetocrystalline anisotropy (MCA), have been investigated via vibrating sample magnetometry (VSM).

II. EXPERIMENTAL DETAILS

Preparation and characterization of the thin oxide films were carried out in an interconnected ultrahigh-vacuum (UHV) system at a base pressure of 10^{-8} mbar in the deposition chamber and 10^{-10} mbar in the analysis chamber. Epitaxial Fe_3O_4/NiO ultra thin bilayer systems with thicknesses between 5 nm and 20 nm were grown via reactive molecular beam epitaxy (RMBE) on 0.05 % Nb-doped $SrTiO_3$(001) or on MgO(001) single crystalline substrates. Prior to deposition, the substrates were annealed at 400 °C in 1×10^{-4} mbar O_2 atmosphere for 1 h in order to remove carbon contamination and get well-defined surfaces. Subsequently, nickel oxide and magnetite films were deposited by thermal evaporation from pure metal rods in 1×10^{-5} mbar and 5×10^{-6} mbar oxygen atmosphere, respectively. Deposition was performed at 250 °C substrate temperature using deposition rates of 0.01 nm/s for nickel oxide films and 0.25 nm/s for magnetite films as controlled by a quartz microbalance adjacent to the evaporation source. The resulting film thicknesses were determined later on *ex situ* by XRR. Crystal surface quality and stoichiometry were controlled

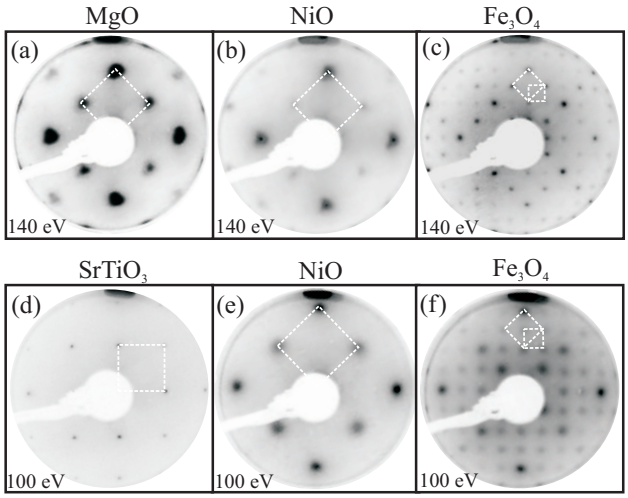

FIG. 1: LEED pattern recorded at 140 eV for (a) pure MgO(001) surface, (b) 11.9 nm NiO film on MgO(001) and (c) 21.5 nm Fe_3O_4 on NiO/MgO(001). The LEED pattern taken at 100 eV of a pure $SrTiO_3$ surface, a 10.4 nm NiO film on $SrTiO_3$(001) and 20.7 nm Fe_3O_4 on NiO/$SrTiO_3$(001) are depicted in (d), (e) and (f), respectively. The larger white square indicates (1×1) structure of the reciprocal unit cell of the respective surface while the smaller white square in (c) and (f) indicates the $(\sqrt{2}\times\sqrt{2})R45°$ superstructure unit cell of magnetite.

in situ after each preparation step by LEED and XPS using an Al K_α ($h\nu$ = 1486.6 eV) radiation source and a Phoibos HSA 150 hemispherical analyzer.

After transport under ambient conditions XRR and XRD experiments were carried out *ex situ* for structural characterization of the films. XRR measurements were performed in θ-2θ geometry using a lab based diffractometer (Philips XPert Pro) equipped with a Cu K_α anode. An in-house developed fitting tool based on the Parratt algorithm [36] using Névot-Croce [37] roughness profiles was applied for the analysis of the XRR curves. For XRD synchrotron based radiation sources at the MaXLab beamline I811 (MaXLab, Lund, Sweden) and at the Swiss Light Source beamline X04SA (Paul Scherrer Institute, Villigen, Switzerland) were used. Both beamlines are equipped with (2S + 3D) type diffractometers and Pilatus pixel area detectors for data collection. The XRD data were recorded in θ-2θ geometry at an energy of 12.4 keV and analyzed within the full kinematic diffraction theory [38] using an in-house developed fitting tool.

In addition, the magnetization curves were measured at room temperature for several in-plane directions of the samples by varying the magnetic field $\mu_0 H$ between -300 mT and +300 mT, using a vibration sample magnetometer (VSM, Lakeshore, Model 7407). The magnetization loops were corrected by subtracting the paramagnetic contribution from the substrates.

III. RESULTS

A. LEED / XPS

Figure 1 presents the LEED pattern of the cleaned MgO(001) and $SrTiO_3$(001) surfaces and the as prepared oxide films on the respective substrate. Exemplarily, only patterns of a $\sim$ 20 nm Fe_3O_4 and $\sim$ 10 nm NiO films are shown due to similar results. The intensity variations in all recorded patterns are due to dynamical scattering for electron diffraction.

Clear (1×1) structures corresponding to the square unit cells of MgO(001) and $SrTiO_3$(001) surfaces can be seen (cf. Fig. 1(a) and (d)). Due to the rocksalt structure of MgO the reciprocal unit vectors of the MgO(001) surface point in [110] and [$\bar{1}$10] directions forming a quadratic reciprocal unit cell. The reciprocal unit vectors of the (001) surface of the perovskite $SrTiO_3$, however, point in [100] and [010] directions forming a quadratic unit cell, as well. Consequently, the reciprocal surface unit vectors of MgO(001) are $\sim \sqrt{2}$ times larger than those of $SrTiO_3$(001).

The diffraction spots of the $SrTiO_3$ pattern are sharp and intense while the spots of the MgO substrate are broadened due to charging effects. The diffuse background is quite low in both patterns pointing to clean surfaces and negligible point defects. Additional, XPS measurements of both substrates show no carbon contamination indicating chemically clean substrates.

After deposition of NiO the LEED patterns exhibit a (1×1) structure related to the square symmetry of the NiO(001) surface for both substrates (cf. Fig. 1(b) and (e)). As mentioned above, due to the rocksalt structure, the reciprocal unit vectors of NiO(001) surface point in [110] and [$\bar{1}$10] directions and are consequently $\sim \sqrt{2}$ times larger than the surface unit cell of $SrTiO_3$ in reciprocal space. Due to the very similar lattice constants of NiO(001) and MgO(001) the diffraction spots are located at almost identical positions compared to MgO(001) pattern. The bright diffraction spots and negligible background intensity of the NiO(001) surface also indicate a good crystalline quality with long range order for the growth on both substrates. However, compared to the diffraction pattern of the NiO/MgO, the diffraction spots of the NiO/$SrTiO_3$ surface are slightly broadened. This effect can be related to the formation of defects induced by the high lattice misfit of - 6.9 % for NiO(001) on $SrTiO_3$(001).

The LEED images of Fe_3O_4 obtained after deposition on NiO/MgO(001) and NiO/$SrTiO_3$(001) show similar diffraction patterns with a square symmetry (cf. Fig. 1(c) and (f)). Clear diffraction spots with half peak distance compared to the NiO(001) surface indicate approximately doubled lattice constant in real space due to the almost doubled cubic lattice constant of Fe_3O_4 compared to the other oxides used here. Furthermore, an additional $(\sqrt{2} \times \sqrt{2})R45°$ superstructure appears which is characteristic for a well-ordered magnetite surface [39–41]. This superstructure is not observed for maghemite (Fe_2O_3) which has a very similar surface lattice constant. Therefor, we assume a formation of well-ordered stoichiometric magnetite films. The bright diffraction spots and the low background intensity verify a low defect density and large crystalline areas of the magnetite films for both substrates. The broadening of the diffraction spots of the magnetite surface grown on NiO/$SrTiO_3$(001) can be attributed to the already defective NiO surface caused by the high lattice mismatch.

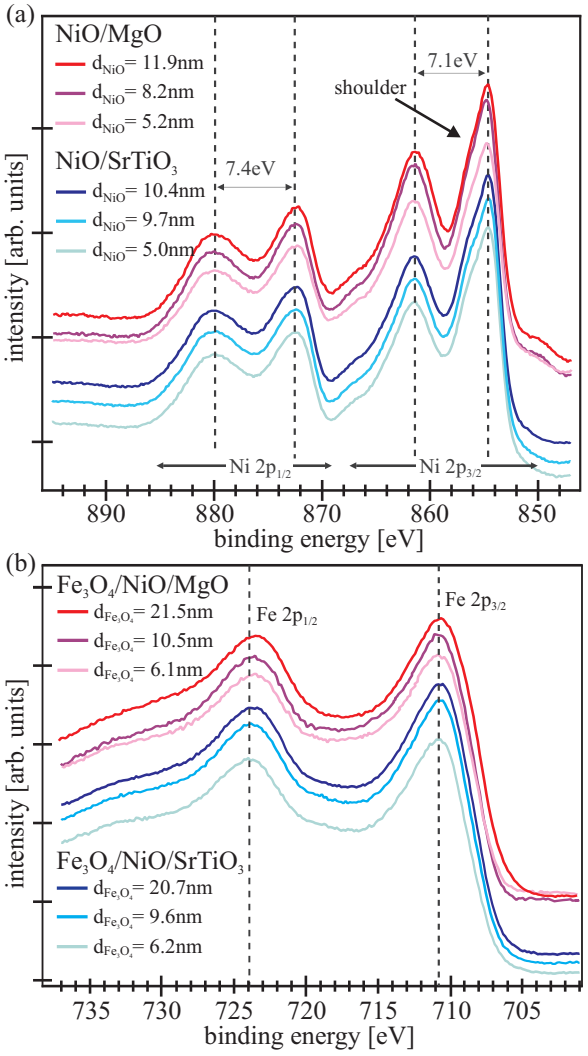

FIG. 2: X-ray photoelectron spectra of (a) Ni 2p region for the as prepared NiO films on MgO(001) and $SrTiO_3$. (b) Fe 2p region for the as prepared Fe_3O_4 films on NiO/MgO(001) and NiO/$SrTiO_3$.

In summary, the LEED patterns of the Fe_3O_4/NiO bilayer systems confirm a crystalline cube on cube growth of both NiO and Fe_3O_4 films on MgO(001) as well as on $SrTiO_3$(001). The films grown on MgO substrates exhibit a higher crystalline quality and less surface defects compared to the bilayers grown on $SrTiO_3$.

XPS measurements were made directly after deposi-

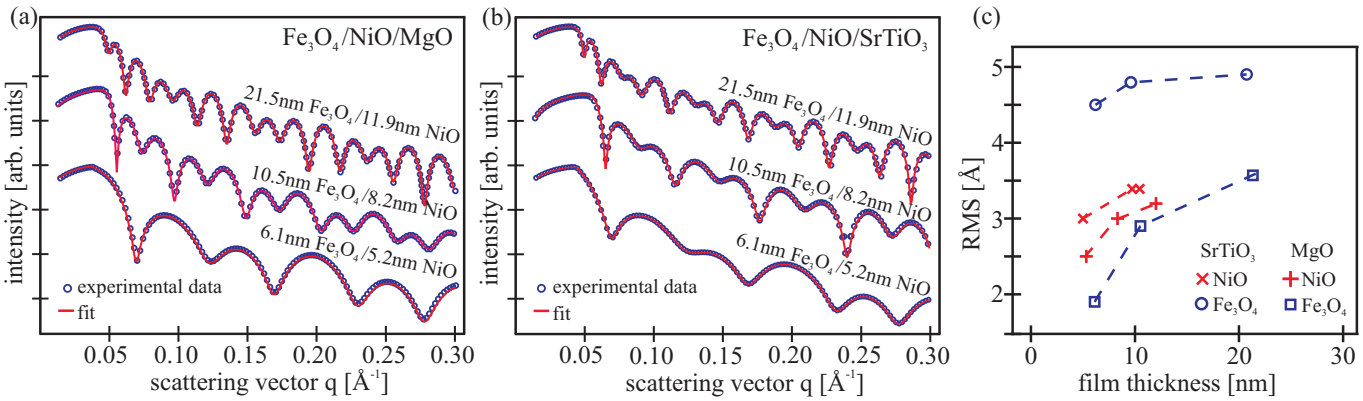

FIG. 3: XRR measurements and the calculated intensities of the bilayers on (a) MgO and (b) $SrTiO_3$ substrates. (c) Surface and interface roughnesses obtained from the XRR measurements.

tion of the films to determine the stoichiometry and the valence state of the cation species. Figure 2(a) shows the XP spectra of the Ni 2p region after deposition of nickel oxide and before deposition of iron oxide. All spectra of the Ni 2p core level reveal Ni $2p_{3/2}$ and Ni $2p_{1/2}$ peaks at binding energies of 854.6 eV and 872.5 eV, respectively, and two intense satellite structures at about 7 eV higher binding energies. Since these values agree well with the binding energies reported in literature for a Ni^{2+} valence state in NiO stoichiometry [42, 43] we assume that the oxide films are stoichiometric and have negligible amounts of point defects as, e.g., oxygen vacancies. Additionally, there is a shoulder ∼1.5 eV above the Ni $2p_{3/2}$ peak, which is reported to be typical for NiO [44, 45]. Thus, the shape of all spectra is comparable to that of NiO bulk crystal [43, 46, 47].

In Figure 2(b), the Fe 2p photoelectron spectra of the iron oxide films as prepared on top of the NiO films are presented. From the position and shape of the Fe 2p peaks one can get information about the iron oxidation state and the stoichiometry. All recorded spectra exhibit the same shape with main peaks located at binding energy 710.6 eV and 723.6 eV for Fe $2p_{3/2}$ and Fe $2p_{1/2}$, respectively. These binding energies of the core levels correspond to values of Fe_3O_4 well-known from literature [48]. Additionally, in contrast to wüstite (FeO) and maghemite (Fe_2O_3), no apparent charge transfer satellites can be observed between the two main peaks due to their overlap [48, 49]. Consequently, all prepared iron oxide films exhibit the desired Fe_3O_4 stoichiometry. Thus, both XPS and LEED measurements demonstrate that the bilayer structures on both kind of substrates consist of crystalline stoichiometric NiO and Fe_3O_4 films.

B. XRR / XRD

XRR and XRD experiments were performed *ex situ* to determine the structural parameters of the bilayers, e.g., film thicknesses and vertical lattice distances. Figures 3(a) and 3(b) show the measured reflectivity curves and the corresponding calculated reflectivity curves after optimizing the structural parameters. In addition, the obtained thicknesses of all studied bilayers are presented. For all samples clear intensity oscillations with beating effects are visible indicating double layer structures and flat homogenous films with small interface and surface roughness.

The applied calculation model consists of a layer of iron oxide on top of a nickel oxide layer on MgO or $SrTiO_3$ substrate. All fitted curves agree excellently with the experimental data using literature values for the dispersion $\delta_{Fe_3O_4} = 1.53 \times 10^{-6}$ and $\delta_{NiO} = 1.89 \times 10^{-6}$ [50]. This indicates a small defect density, e.g., oxygen vacancies which is in accordance with the XPS results.

Additionally, the roughnesses of the films were determined and are presented in Fig. 2(c). Here, all films feature an increase of the surface and interface roughness with increasing film thickness. This effect can be attributed to kinetic roughening of the films during growth and to the progressing relaxation process [51]. The nickel oxide films exhibit similar roughnesses of $\sigma_{NiO} = 2.5$ - 3.5 Å on both substrates with small increase for thicker films. The roughness of the Fe_3O_4 on NiO/MgO increases more drastically, while the magnetite films deposited on NiO/$SrTiO_3$ show nearly constant large roughness with initially almost doubled values compared to the magnetite films on NiO/MgO. This behavior is likely caused by high lattice misfit and the resulting relaxation process. It is in accordance with the broadened diffraction spots of the Fe_3O_4 films on NiO/$SrTiO_3$ observed in the LEED pattern (cf. Fig. 1).

Figures 4(a) and 4(b) present the SR-XRD measurements of the (00L) crystal truncation rod (CTR) compared to intensities calculated by kinematic diffraction theory of the Fe_3O_4/NiO bilayers on MgO(001) and $SrTiO_3$(001), respectively. Here, the bulk nomenclature of the reciprocal space was used, where $L = c\,K_\perp/(2\,\pi)$ in reciprocal lattice units (r.l.u.) denotes the vertical scattering vector $K_\perp$ scaled to the Bragg condition $2\,\pi/c$

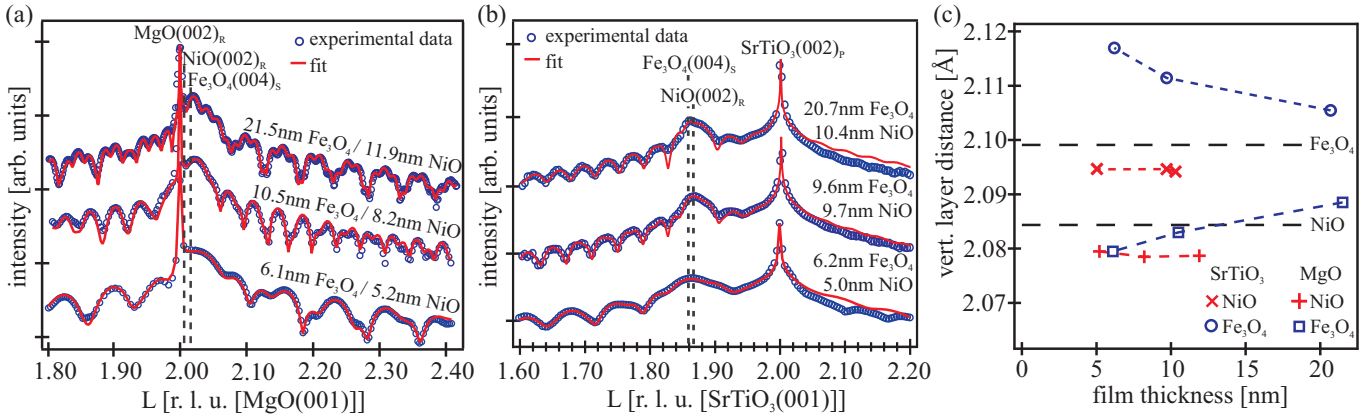

FIG. 4: XRD measurement along the $(00L)$ CTR (a) of the Fe_3O_4/NiO/MgO samples and (b) of the Fe_3O_4/NiO bilayers on $SrTiO_3$. In red the calculated intensity distribution using the kinematic approximation is shown. (c) Vertical layer distance of nickel oxide and magnetite grown on MgO(001) and $SrTiO_3$(001) dependent on the film thickness. The dotted lines denote the fully relaxed bulk values of magnetite and nickel oxide.

($c_{MgO} = 4.2117$ Å, $c_{SrTiO_3} = 3.905$ Å). Due to the almost doubled lattice constant of magnetite compared to both MgO and NiO and the resulting lateral tensile strain, the $(004)_S$ spinel bulk reflection is located at higher L values compared to MgO and close to the $(002)_R$ bulk reflection of a rock salt structure. On $SrTiO_3$, both nickel oxide and magnetite exhibit a large lattice misfit and are laterally compressively strained. Thus, the $(004)_S$ reflection of magnetite and $(002)_R$ reflection of NiO are at lower L values compared to $SrTiO_3$ and well separated from the $(002)_P$ perovskite reflection of $SrTiO_3$. Here, the indexes R, S and P indicate bulk indexing for rock salt, spinel and perovskite type, respectively.

For all bilayers grown on MgO, the measurements show a sharp peak at $L = 2$ originating from the diffraction at the MgO substrate lattice (cf. Fig. 4(a)). Additionally, broad rather intense features located at $L \sim 2.02$ accompanied by strong Laue oscillations are visible due to finite thickness of the iron and nickel oxide. The well-pronounced intensity oscillations with two superposed partial oscillations clearly show a periodicity of two layers of different thickness indicating a high crystalline ordering and homogenous thicknesses of both films, magnetite and nickel oxide. This is in accordance with the results seen in the XRR measurements.

In the case of bilayers grown on $SrTiO_3$, the $(00L)$ rod also shows a sharp substrate peak at $L = 2$ and Laue oscillations due to crystalline magnetite and nickel oxide films (cf. Fig. 4(b)). Here, the Bragg peaks originating from the iron and nickel oxide are located at $L \sim 1.86$ and broadened due to the finite film thicknesses. On closer inspection, the Laue oscillations show also a periodicity of two layers whereby the damping of the oscillation originating from the magnetite increases with increasing magnetite thickness due to increasing roughness of the Fe_3O_4 films (cf. Fig. 3(c)).

Due to the small lattice mismatch between Fe_3O_4 and NiO a separation of the Bragg peaks originating from the respective film is not visible by eye. Complete data analysis using fully kinematic diffraction theory was performed to obtain the vertical layer distance of the respective oxide film. Within the calculation the atomic form factors of oxygen, nickel and iron arranged in a bulk structure are kept constant while the vertical size of the unit cell is varied. The applied models consist of a homogenous Fe_3O_4/NiO bilayer on top of the respective substrate. This structural model involving the number of layers coincides with the layer model and the film thicknesses obtained from XRR calculations. The obtained vertical layer distances ($c_{NiO}/2$ for NiO and $c_{Fe_3O_4}/4$ for Fe_3O_4) are shown in Fig. 4(c).

The dotted lines mark the bulk values of the magnetite and nickel oxide. Due to a larger unit cell of MgO(001) pseudomorphic growth of NiO on MgO results in an expansion of the NiO unit cell in lateral direction and, thus, a vertical compression and consequently a smaller vertical lattice distance. In the case of NiO grown on $SrTiO_3$(001) exactly the opposite is expected due to a smaller bulk unit cell of $SrTiO_3$ compared to NiO resulting in an expansion of the vertical unit cell of NiO.

For the NiO layers on MgO the vertical layer distance exhibits a compressive strain (2.078 Å) and shows no dependence on the NiO thickness in the investigated range (cf. Fig. 4(c)). In the case of bilayers grown on $SrTiO_3$ the vertical lattice distance of NiO (2.095 Å) points to tensile strain as a result of the lateral compression. Further, there is no dependence on the NiO thickness, as well.

However, the situation is different for the relaxation of the magnetite films. Due to pseudomorphic growth of NiO on MgO the vertical layer distance of Fe_3O_4 grown on top of NiO/MgO is also slightly compressively strained but relaxes to higher values with increasing magnetite thickness. Its value relaxes from 2.0795 Å for the 6.1 nm thick magnetite film to 2.0885 Å for the thickest magnetite film. A strong relaxation with increasing film

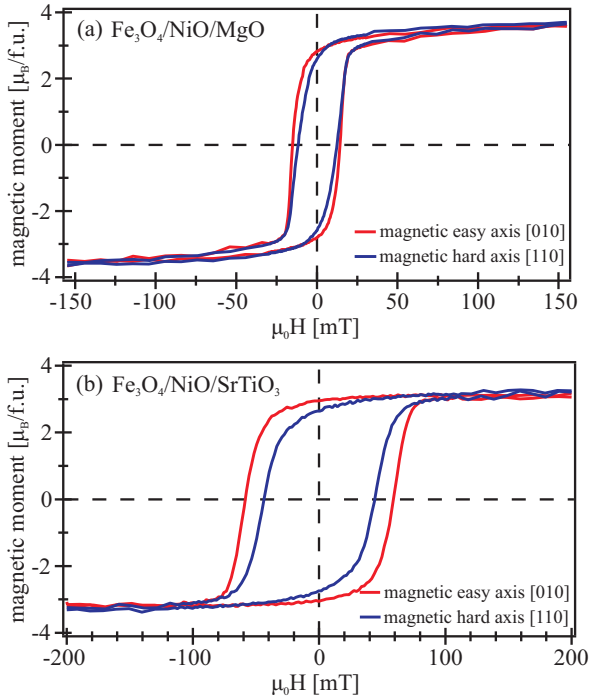

FIG. 5: VSM magnetization curves of magnetic easy and hard direction for (a) 21.5 nm thick Fe_3O_4 film on NiO/MgO and (b) 20.7 nm thick Fe_3O_4 film on $NiO/SrTiO_3$.

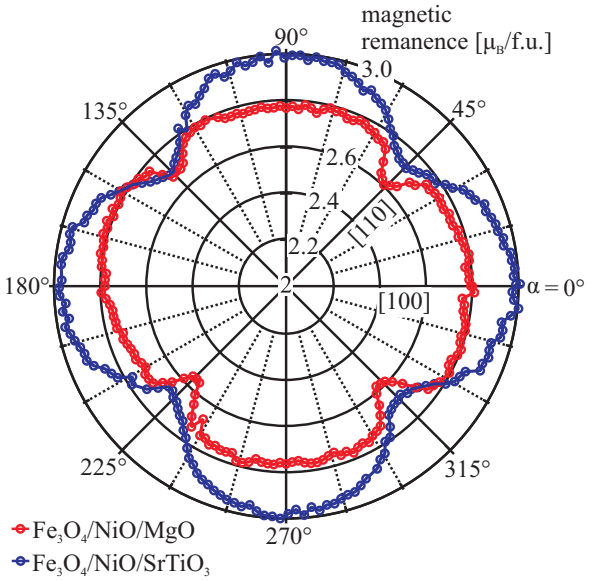

FIG. 6: Polar plots of the magnetic remanence dependent on the azimuthal sample angle α of a 21.5 nm thick Fe_3O_4 film on NiO/MgO (red) and 20.7 nm thick Fe_3O_4 film on $NiO/SrTiO_3$ (blue).

thickness of the magnetite can also be seen for magnetite films grown on $NiO/SrTiO_3$. The vertical lattice distance of Fe_3O_4 on $NiO/SrTiO_3$ is heavily tensile strained and decreases rapidly from 2.117 Å for the thinnest film to 2.106 Å for the 20.7 nm thick magnetite film.

C. VSM

Exemplary, the magnetic properties of the two thickest magnetite films on NiO/MgO and $NiO/SrTiO_3$ were studied by means of VSM. The magnetization curves were measured for different azimuthal sample directions α between the substrate [100] direction and the applied magnetic field. Figures 5(a) and 5(b) show the magnetic moment per f.u. as a function of the magnetic field for the bilayers on MgO and $SrTiO_3$, respectively, for two different directions of the external magnetic field. For both samples a typical ferro(i)magnetic behavior can be observed. Here, the blue curves recorded with the magnetic field applied in [110] direction of the substrates represent magnetic easy axes with a high magnetic remanence and coercive fields. The red curves recorded with the magnetic field applied in [010] direction exhibit the magnetic behavior of a magnetic hard axis due to a lower strength of the coercive field and a smaller magnetic remanence.

The Fe_3O_4 film on $NiO/SrTiO_3$ show an enhanced coercive field compared to the magnetite film grown on NiO/MgO. One possible reason could be a higher density of grain boundaries due to the relaxation process, which supports pinned multidomain states that need larger magnetic fields to be switched. This is consistent with the weaker structural quality, e.g., high roughness, broad diffraction peaks, seen in the LEED, XRR and XRD measurements. Further, the saturation magnetization of the Fe_3O_4 film grown on NiO/MgO amounts to $(3.7\pm0.3)\,\mu_B$/f.u. and coincides with the expected value of $4.0\,\mu_B$/f.u. within the error tolerance [52, 53]. In contrast, magnetite on $NiO/SrTiO_3$ shows a lower magnetic moment of $(3.3\pm0.3)\,\mu_B$/f.u., which may result from the antiferromagnetic coupling in the vicinity of anti-phase domain boundaries (APBs) [54].

The remanent magnetization as a function of azimuthal sample angle α is shown in Fig. 6 for both investigated samples. The maxima of the magnetic remanence point into ⟨100⟩ directions for both Fe_3O_4 films on NiO/MgO and $NiO/SrTiO_3$ indicating the magnetic easy directions. Consequently, the magnetic hard axes are located in ⟨110⟩ directions.

IV. DISCUSSION

XPS measurements taken directly after deposition reveal stoichiometric Fe_3O_4 and NiO on both substrates independent of the film thicknesses. Due to the limited mean free path of the electrons only the surface near region (∼5 nm) of the layers could be characterized. In this region no evidence for the formation of non stoichiometric magnetite was observed. Pilard *et al.* found a 1.5 nm thick $NiFe_2O_4$ interfacial layer after depositing NiO above 610 °C on Fe_3O_4 [32]. Within the XPS mea-

surements presented here the interfacial region could be detected only for the thinnest magnetite films showing spectral shape and binding energies typical for Ni^{2+} in NiO stoichiometry. Thus, there is no evidence for the formation of $NiFe_2O_4$.

Hard x-ray photoelectron spectroscopy (HAXPES) and x-ray magnetic circular dichroism (XMCD) measurements [33] of the same samples recorded after transport under ambient conditions show small traces of Fe^{3+} excess on the surface of the bilayers grown on $SrTiO_3$. However, in deeper layers and at the interface the presence of stoichiometric NiO and Fe_3O_4 was confirmed excluding the formation of $NiFe_2O_4$ clusters or any interfacial layer also for thicker Fe_3O_4 films [33]. Consequently, very thin magnetite films tend to form maghemite at the surface after exposure to ambient air whereby thicker films seem to be more stable like it was reported before by Fleischer *el al.* [55]. Since XPS and LEED measurements taken after preparation and under UHV conditions show no evidence for maghemite, a capping layer deposited directly after growth could prevent the possible oxidation process in the upper layers.

In situ LEED measurements also verified the Fe_3O_4 stoichiometry of the iron oxide film showing the typical $(\sqrt{2} \times \sqrt{2})R45°$ superstructure of the magnetite surface for all investigated films. Further, NiO films on both substrates exhibit the expected (1×1) pattern due to the rock salt crystal structure. The diffraction spots of the magnetite and NiO films grown on $SrTiO_3$ are slightly broadened compared to the films grown on MgO indicating the formation of surface defects due to the high lattice misfit. Surface roughnesses obtained from the XRR analysis exhibit higher values for all films grown on $SrTiO_3$. But while the roughness of the nickel oxide films deposited on $SrTiO_3$ is only about 0.5 Å higher than after deposition on MgO, the magnetite films on $NiO/SrTiO_3$ show initially almost doubled values compared to the magnetite films on NiO/MgO. This result is consistent with the broadened diffraction spots in the LEED pattern. Nevertheless, the XRR measurements provide distinct intensity oscillations indicating double layer structures and homogenous film thicknesses. Thus, no intermixing of the two layers takes place during the deposition process.

The entire structure of the samples was investigated by XRD measurements of the specular CTR. For all samples the thickness determined by XRR agrees well with the Laue oscillations and, hence, with the number of layers used for the XRD calculation. The strong intensity oscillations reveal crystalline and well-ordered nickel oxide and magnetite films with homogeneous thicknesses on both substrates.

The vertical layer distances of all NiO films show no dependence on the thickness in the investigated range. However, NiO and Fe_3O_4 films grown on MgO exhibit a vertical compressive strain while NiO and Fe_3O_4 films on $SrTiO_3$ show vertical tensile strain due to lattice matching at the interface. Based on elastic theory for continuum the vertical lattice constant c for homogenous tetragonally (in-plane) distorted films can be calculated by using the formula [56]

$$\frac{\Delta c}{c} = \frac{2\nu}{\nu - 1} \frac{\Delta a}{a} \ . \tag{1}$$

For the calculation of the vertical layer distance for a completely strained film Δa from pseudomorphic growth was used. Assuming a Poisson number of $\nu = 0.21$ for NiO [19] the vertical layer distance of pseudomorphic NiO on MgO was calculated to be 2.079 Å, hence, the NiO films grown on MgO are fully strained. Above a critical thickness d_c this strain should reduce rapidly due to the stable formation of dislocations. The critical thickness d_c at which the generation of misfit dislocation will begin can be calculated by the formula [57]

$$\frac{d_c}{b} = \frac{\left(1 - \nu \cos^2 \alpha\right) \left(\ln\left(\frac{d_c}{b}\right) + 1\right)}{2\,\pi\, f\, (1 + \nu)\, \cos(\lambda)} \ . \tag{2}$$

Here, $b = \frac{a_{\mathrm{film}}}{\sqrt{2}}$ is the magnitude of the Burgers vector, f the lattice mismatch ($f = 0.8\%$ for NiO on MgO), ν the Poisson ratio, $\alpha = 90°$ is the angle between the Burgers vector and the dislocation line and $\lambda = 45°$ is the angle between the Burgers vector and the direction both normal to the dislocation line and within the plane of the interface. For NiO films on MgO(001) the critical thickness is determined to 39 nm. Since the studied films are below the critical thickness the absence of strain relaxation is in good agreement with this model. Similar results are also observed by Schemme *et al.* [28] for NiO films of different thicknesses up to 34 nm grown on MgO(001). The experimental data of James *et al.* [19] show a strain relaxation above ∼40 nm which is consistent with our observations and confirms Eq. (2).

Despite, the large misfit of -6.9% between NiO and $SrTiO_3$ the XRD curves of all studied films also feature distinct Laue oscillations pointing to a good crystalline ordering. Assuming a complete lattice matching at the interface we calculate a vertical lattice distance of 2.161 Å for fully strained NiO films on $SrTiO_3$ (Eq. (1)) while we observe a film thickness independent value of 2.095Å. Thus, the remaining lateral strain calculated by Eq. (1) only amounts to -0.6%. For the critical thickness Eq. (2) reveals a value of 3.5 Å. All prepared NiO films are well above the critical thickness so the observed strong strain relaxation seems to be reasonable although they are not completely relaxed. We assume that the residual strain cannot be removed from the film due to kinetic difficulties.

In the case of Fe_3O_4 on NiO/MgO, we obtain a vertical layer distance for a fully strained film of 2.092 Å and a critical thickness of 105 nm ($\nu = 0.356$ [58], $f = 0.3\%$) applying Eq. (1) and Eq. (2), respectively. Here, the misfit f coincides with the misfit of magnetite on MgO since the growth of NiO on MgO is pseudomorph adapting its lateral lattice constant. All our investigated magnetite films on NiO/MgO are strongly strained having a

lower vertical layer distance than calculated by Eq. (1) for pseudomorphic films. Furthermore, the films relax with increasing magnetite thickness, although the predicted critical thickness is far from being reached. This behavior also coincides with the results reported by Schemme *et al.* [28], but cannot be explained so far.

Though the low remaining strain of only -0.6% between the Fe_3O_4 and $NiO/SrTiO_3$, these magnetite films are less structurally ordered than the magnetite films grown on NiO/MgO. While the crystalline quality of the NiO films on $SrTiO_3$ is constantly high independent of the film thickness, the strength of Laue oscillations of the Fe_3O_4 films grown on top of $NiO/SrTiO_3$ decreases with increasing magnetite thickness. This result is supported by the high surface roughness of the magnetite films obtained from the XRR measurements as well as by the broadened diffraction spots seen in the LEED pattern. One reason for this behavior could be the fast relaxation process and consequently the formation of grain boundaries and structural defects, e.g., APBs during the initial stage of film growth. The vertical layer distance of a fully strained film and the critical thickness for the formation of misfit dislocations assuming a remaining lattice mismatch of -1% at the interface to the partially relaxed NiO is calculated to be 2.123 Å and 27 nm using Eq. (1) and Eq. (2), respectively. The measured value of 2.117 Å for the 5 nm thick magnetite film is already lower than the expected value for pseudomorphic growth. With increasing magnetite thickness the measured vertical layer distance strongly relaxes to 2.104 Å for the 20.7 nm thick film although the critical thickness is not reached. This coincides with the observations made for Fe_3O_4 films grown NiO/MgO. Therefore, it seems that elasticity theory overestimates the formation energy of dislocations in the magnetite film.

VSM measurements of the two thickest magnetite films on NiO/MgO and $NiO/SrTiO_3$ reveal ferro(i)magnetic behavior for both samples. However, the Fe_3O_4 film grown on $NiO/SrTiO_3$ shows enhanced coercive field compared to the film on NiO/MgO possibly caused by a higher density of grain boundaries and, thus, a formation of more pinning centers. This behavior coincides with the weaker structural ordering and a higher surface roughness of the magnetite films on $NiO/SrTiO_3$ seen in the LEED, XRD and XRR measurements. An increased coercive field for magnetite films grown on $SrTiO_3$ caused by a higher surface roughness or strain have also been reported in Refs. [59, 60].

The obtained saturation magnetization values of Fe_3O_4 grown on NiO/MgO and $NiO/SrTiO_3$ coincide within the error tolerances with the values determined by XMCD [33]. Additionally, the value of Fe_3O_4 film on NiO/MgO is also rather close to the ideal theoretical value as well as to experimental bulk moment of magnetite of $4.07\mu_B$/f.u. [52, 53, 61], whereas Fe_3O_4 on $NiO/SrTiO_3$ exhibits a lower value. A reduced magnetic moment has also been reported for $Fe_3O_4/SrTiO_3$ systems possibly caused by a large density of APBs induced by high lattice mismatch [29, 62]. This result is supported by a weaker structural ordering as well as higher coercive fields and, thus, a higher density of grain boundaries observed for Fe_3O_4 on $NiO/SrTiO_3$.

Further, both investigated samples show a fourfold magnetic in-plane anisotropy with magnetic easy axes aligned along the ⟨100⟩ directions. However, for thin magnetite films on MgO(001) the magnetic easy axes are reported to point into ⟨110⟩ directions [63, 64], while for Fe_3O_4 films on $SrTiO_3$(001) the magnetic easy axes are pointing into ⟨100⟩ directions, as well [30, 59]. In this case, a tetragonal distortion of the films can influence the spin-orbit coupling which may lead to modified MCA constants and, thus, altered directions of magnetic easy and hard axes. Moreover, magnetite films grown on an iron buffer layer exhibit a magnetic in-plane anisotropy with magnetic easy axes parallel to ⟨100⟩ [65]. Thus, a modified interface of the Fe_3O_4 films can lead to a rotation of the magnetic in-plane anisotropy and influence the magnetic properties of magnetite.

V. SUMMARY

We present a comparative study on the structural and magnetic properties of Fe_3O_4/NiO bilayers grown on MgO(001) and Nb-doped $SrTiO_3$(001). Stoichiometric magnetite and NiO films with a homogenous thicknesses were found on both substrates in the investigated thickness range (5-20 nm). Detailed analysis of the XRD measurements reveal a high crystallinity of the NiO films independent of the underlying substrate or film thickness. However, magnetite films grown on $NiO/SrTiO_3$ exhibit a weaker structural ordering and higher surface roughness compered to the films grown on NiO/MgO induced by a large lattice mismatch and the resulting relaxation process. Further, the bilayers exhibit a vertical compressive strain on MgO but a tensile strain in vertical direction on $SrTiO_3$ as a result of lateral compression. The weak crystalline structure of Fe_3O_4 on $NiO/SrTiO_3$ affects the magnetic properties leading to an enhanced coercive field and a reduced magnetic moment compared to magnetite on NiO/MgO. Nevertheless, these Fe_3O_4/NiO bilayers on MgO and $SrTiO_3$ substrates are expected to show large thermoelectric effects based on the thermal generation of spin currents (spin Seebeck effect) [10–12] supported by the antiferromagnetic NiO layer [20, 21].

Additionally, both systems show a fourfold magnetic in-plane anisotropy with magnetic easy axes pointing in ⟨100⟩ directions which is 45° rotated to the well known magnetic easy axes directions of thin magnetite films. One potential reason may be a modified spin-orbit coupling as a result of the tetragonal distortion of the films leading to altered magnetocrystalline anisotropy. A detailed understanding of these bilayers is of utmost importance since they are excellent candidates for potential spintronic and spincaloritronic applications. Therefore, this behavior deserves further future stud-

ies including high resolution TEM investigation to shed more light on this interesting change of the magnetic anisotropy of Fe_3O_4 thin films grown on NiO/MgO(001) and NiO/$SrTiO_3$(001).

Acknowledgments

The authors gratefully acknowledge the financial support by the Deutsche Forschungsgemeinschaft (DFG) via grants No. KU2321/2-1 and KU3271/1-1. Portions of this research were carried out at beamline I811, MaXLab synchrotron radiation source, Lund University, Sweden. Funding for the beamline I811 project was kindly provided by The Swedish Research Council and The Knut och Alice Wallenbergs Stiftelse. Additional experiments were performed at the X04SA beamline at the Swiss Light Source synchrotron radiation source at Paul Scherrer Institute, Villigen, Switzerland. We like to thank the I811 and X04SA beamline staff for experimental support.

[1] C. N. R. Rao, Annu. Rev. Phys. Chem. **40**, 291 (1989).
[2] J.-B. Moussy, J. Phys. D: Appl. Phys. **46**, 143001 (2013).
[3] A. Hoffman and S. D. Bader, Phys. Rev. Applied **4**, 047001 (2015).
[4] G. E. W. Bauer, E. Saitoh, and B. J. van Wees, Nat. Mater. **11**, 391 (2012).
[5] Z. Zhang and S. Satpathy, Phys. Rev. B **44**, 13319 (1991).
[6] R. Cornell and U. Schwertmann, *The Iron Oxides: Structure, Properties, Reactions, Occurences and Uses* (Wiley-VCH GmbH & Co. KGaA, 2003).
[7] P. Seneor, A. Fert, J.-L. Maurice, F. Montaigne, F. Petroff, and A. Vaurés, Appl. Phys. Lett. **74**, 4017 (1999).
[8] T. Kado, Appl. Phys. Lett. **92**, 092502 (2008).
[9] E. Wada, K. Watanabe, Y. Shirahata, M. Itoh, M. Yamaguchi, and T. Taniyama, Appl. Phys. Lett. **96**, 102510 (2010).
[10] R. Ramos, A. Anadón, I. Lucas, K. Uchida, P. A. Algarabel, L. Morellón, M. H. Aguirre, E. Saitoh, and M. R. Ibarra, APL Materials **4**, 104802 (2016).
[11] R. Ramos, T. Kikkawa, K. Uchida, H. Adachi, I. Lucas, M. H. Aguirre, P. Algarabel, L. Morellón, S. Maekawa, E. Saitoh, et al., Appl. Phys. Lett. **102**, 072413 (2013).
[12] K.-I. Uchida, H. Adachi, T. Kikkawa, A. Kirihara, M. Ishida, S. Yorozu, S. Maekawa, and E. Saitoh, Proc. IEEE **104**, 1946 (2016).
[13] E. J. W. Verwey, Nature **144**, 327 (1939).
[14] J. Yoshida and S. Iida, J. Phys. Soc. Jpn. **42**, 230 (1977).
[15] K. Kato and S. Iida, J. Phys. Soc. Jpn. **51**, 1335 (1982).
[16] M. Alexe, M. Ziese, D. Hesse, P. Esquinazi, K. Yamauchi, T. Fukushima, S. Picozzi, and U. Gsele, Adv. Mater. **21**, 4452 (2009).
[17] W. H. Meiklejohn and C. P. Bean, Phys. Rev. **102**, 1413 (1956).
[18] G. Srinivasan and M. S. Seehra, Phys. Rev. B **29**, 6295 (1984).
[19] M. James and T. Hibma, Surf. Sci. **433-435**, 718 (1999).
[20] W. Lin, K. Chen, S. Zhang, and C. L. Chien, Phys. Rev. Lett. **116**, 186601 (2016).
[21] A. Prakash, J. Brangham, F. Yang, and J. P. Heremans, Phys. Rev. B **94**, 014427 (2016).
[22] F. Bertram, C. Deiter, T. Schemme, S. Jentsch, and J. Wollschläger, J. Appl. Phys. **113**, 184103 (2013).
[23] S. K. Arora, H.-C. Wu, R. J. Choudhary, I. V. Shvets, O. N. Mryasov, H. Yao, and W. Y. Ching, Phys. Rev. B **77**, 134443 (2008).
[24] S. K. Arora, R. G. S. Sofin, I. V. Shvets, and M. Luysberg, J. Appl. Phys. **100**, 073908 (2006).
[25] H.-C. Wu, R. Ramos, R. G. S. Sofin, Z.-M. Liao, M. Abid, and I. V. Shvets, Appl. Phys. Lett. **101**, 052402 (2012).
[26] C. Gatel, E. Snoeck, V. Serin, and A. R. Fert, Eur. J. Phys. B **45**, 157 (2005).
[27] H.-C. Wu, S. K. Arora, O. N. Mryasov, and I. V. Shvets, Appl. Phys. Lett. **92**, 182502 (2008).
[28] T. Schemme, O. Kuschel, F. Bertram, K. Kuepper, and J. Wollschläger, Thin Solid Films **589**, 526 (2015).
[29] Y. Z. Chen, J. R. Sun, Y. N. Han, X. Y. Xie, J. Shen, C. B. Rong, S. L. He, and B. G. Shen, J. Appl. Phys. **103**, 07D703 (2008).
[30] M. Monti, M. Sanz, M. Oujja, E. Rebollar, M. Castillejo, F. J. Pedrosa, A. Bollero, J. Camarero, J. L. F. Cunado, N. M. Nemes, et al., J. Appl. Phys. **114**, 223902 (2013).
[31] O. Kuschel, R. Buß, W. Spiess, T. Schemme, J. Wöllermann, K. Balinski, A. T. N'Diaye, T. Kuschel, J. Wollschläger, and K. Kuepper, Phys. Rev. B **94**, 094423 (2016).
[32] M. Pilard, O. Ersen, S. Cherifi, B. Carvello, L. Roiban, B. Muller, F. Scheurer, L. Ranno, and C. Boeglin, Phys. Rev. B **76**, 214436 (2007).
[33] K. Kuepper, O. Kuschel, N. Pathé, T. Schemme, J. Schmalhorst, A. Thomas, E. Arenholz, M. Gorgoi, R. Ovsyannikov, S. Bartkowski, et al., Phys. Rev. B **94**, 024401 (2016).
[34] I. P. Krug, F. U. Hillebrecht, M. W. Haverkort, A. Tanaka, L. H. Tjeng, H. Gomonay, A. Fraile-Rodrguez, F. Nolting, S. Cramm, and C. M. Schneider, Phys. Rev. B **78**, 064427 (2008).
[35] H.-Q. Wang, W. Gao, E. I. Altman, and V. E. Heinrich, J. Vac. Sci. Technol. A **22**, 1675 (2004).
[36] L. Parratt, Rev. Mod. Phys. **95**, 359 (1954).
[37] L. Névot and P. Croce, Rev. Phys. Appl. **15**, 761 (1980).
[38] J. Als-Nielsen and D. McMorrow, *Elements of Modern X-ray Physics* (John Wiley & Sons, Ltd, 2001).
[39] R. Pentcheva, W. Moritz, J. Rundgren, S. Frank, D. Schrupp, and M. Scheffler, Surf. Sci. **602**, 1299 (2008).
[40] J. Korecki, B. Handke, N. Spiridis, T. Slezak, F. Flis-Kabulska, and J. Haber, Thin Solid Films **412**, 14 (2002).
[41] J. F. Anderson, M. Kuhn, U. Diebold, K. Shaw, P. Stoyanov, and D. Lind, Phys. Rev. B **56**, 9902 (1997).
[42] H. Nesbitt, D. Legrand, and G. Bancroft, Phys. Chem. Miner. **27**, 357 (2000).
[43] A. P. Grosvenor, M. C. Biesinger, R. S. C. Smart, and N. S. McIntyre, Surf. Sci. **600**, 1771 (2006).
[44] S. Uhlenbrock, C. Scharfschwerdtt, M. Neumannt, G. Illing, and H.-J. Freund, J. Phys. Condens. Matter **4**, 7973 (1992).

[45] L. Soriano, I. Preda, A. Gutiérrez, and S. Palacín, Phys. Rev. B **75**, 233417 (2007).
[46] A. N. Mansour, Surf. Sci. Spectra **3**, 231 (1994).
[47] A. Carley, S. Jackson, J. N. OShea, and M. W. Roberts, Surf. Sci. Lett. **440**, L868 (1999).
[48] T. Yamashita and P. Hayes, Appl. Surf. Sci. **254**, 2441 (2008).
[49] T. Fujii, F. M. F. de Groot, G. A. Sawatzky, F. C. Voogt, T. Hibma, and K. Okada, Phys. Rev. B **59**, 3195 (1999).
[50] B. Henke, E. Gullikson, and J. Davis, Atom. Data Nucl. Data **54**, 181 (1993).
[51] A. Pimpinelli and J. Villain, *Physics of Crystal Growth* (Campbridge University Press, 1998).
[52] Z. Zhang and S. Satpathy, Phys. Rev. B **44**, 13319 (1991).
[53] H.-T. Jeng and G. Y. Guo, Phys. Rev. B **65**, 094429 (2002).
[54] D. T. Margulies, F. T. Parker, M. L. Rudee, F. E. Spada, J. N. Chapman, P. R. Aitchison, and A. E. Berkowitz, Phys. Rev. Lett. **79**, 5162 (1997).
[55] K. Fleischer, O. Mauit, and I. V. Shvets, Appl. Phys. Lett. **104**, 192401 (2014).
[56] S. Hashimoto, J.-L. Peng, W. Gibson, L. J. Schowalter, and R. W. Fathauer, Appl. Phys. Lett. **47**, 1071 (1985).
[57] J. W. Matthews and A. E. Blakeslee, J. Cryst. Growth **27**, 118 (1974).
[58] A. G. Every and A. K. McCurdy, *Table 7, Cubic System. Binary compounds* (Springer Materials - The Landolt-Boernstein Database , Springer Berlin Heidelberg, 1992).
[59] J. Cheng, G. E. Sterbinsky, and B. W. Wessels, J. Cryst. Growth **310**, 3730 (2008).
[60] J. Dho, B. Kim, and S. Ki, IEEE Trans. Magn. **52**, 2600304 (2016).
[61] P. Weiss and R. Forrer, Ann. d. Phys. **12**, 279 (1929).
[62] G. W. Leung, M. E. Vickers, R. Yu, and M. G. Blamire, J. Cryst. Growth **310**, 5282 (2008).
[63] D. T. Margulies, F. T. Parker, and A. E. Berkowitz, J. Appl. Phys. **75**, 6097 (1994).
[64] T. Schemme, N. Pathé, G. Niu, F. Bertram, T. Kuschel, K. Kuepper, and J. Wollschläger, Mater. Res. Express **2**, 016101 (2015).
[65] T. Schemme, A. Krampf, F. Bertram, T. Kuschel, K. Kuepper, and J. Wollschläger, J. Appl. Phys. **118**, 113904 (2015).